Reducing droplet contact time and area by craterlike surface structure

Chensen Lin,[1] Kaixuan Zhang,[1] Xiaocui Chen,[2] Lanlan Xiao,[3] Shuo Chen,[1,*] Jun Zhu,[4] and Tao Zou[4]

[1]*School of Aerospace Engineering and Applied Mechanics, Tongji University, Shanghai, China*
[2]*College of Energy and Electrical Engineering, Hohai University, Nanjing, China*
[3]*School of Mechanical and Automotive Engineering, Shanghai University of Engineering Science, Shanghai, China*
[4]*Nantong Taisheng Blue Island Offshore CO., Ltd, Nantong, Jiangsu, China*

(Received 30 April 2021; accepted 20 July 2021; published 6 August 2021)

Reduction in contact time and area between the rebounding droplet and the solid surface has attracted great attention due to the potential applications in many fields, such as self-cleaning and anti-icing. In this paper, we provide an alternative strategy for designing a functional surface, craterlike structure, with which the interaction parameter (the integration of contact area over time) can be reduced by over 75%. Systematic investigations on the parameters of craterlike structure, including its diameter, depth, and landing location, have been conducted by a particle-based numerical method, many-body dissipative particle dynamics. This work could be helpful for the design and preparation technology of functional surfaces.

DOI: 10.1103/PhysRevFluids.6.083602

I. INTRODUCTION

Droplets impacting solid surfaces is a key element of a wide variety of phenomena encountered in engineering applications, such as inkjet printing and rapid spray cooling of hot surfaces. What fluid dynamics and heat transfer phenomena occur when a liquid droplet impacts a substrate at a different temperature? Scientists and engineers have been investigating various aspects of this question for more than 100 years [1]. For applications like anti-icing, minimizing the heat exchange at the interface is important.

To reduce the contact between solid and droplet, superhydrophobic surfaces are essential because they tend to bounce off the droplets rather than adhere to them. Recently, people find that manipulating the geometrical pattern of the solid surface is an alternative way to tackle the problem. Bird *et al.* [2] reported that if droplets impact axisymmetrically on a thin ridge, the contact time can be reduced by 37%. The experiments showed the droplet breaks into two parts, and the retraction of the boundary is significantly accelerated. Liu *et al.* [3] have shown that impacts on cylinders whose curvature is comparable to the droplet can reduce the liftoff time up to 40%. Abolghasemibizaki *et al.* [4] showed droplet impact on a cylindrical surface could further reduce the contact time by around 30%. A more astonishing result is reported by Liu *et al.* [5], where the contact time can be reduced by nearly 80% on a tapered texture surface. This is the maximum reduction in the contact time reported to date. Various other studies reported decreased liftoff time through different mechanisms, such as square cavity surface [6], grooves [7], elastic surface [8], etc. From a practical point of view, today's emerging technologies have enabled surface morphology manipulation at the desired scale, thereby increasing the ease of fabricating surfaces with any designed structure [9].

*schen_tju@tongji.edu.cn

Besides the contact time discussed above, the contact area is another essential factor in controlling the contact. The spreading lamella along the substrate can dramatically increase the contact area, thus undermining the reduction effort. Girard *et al.* [10] pointed out the problem and used the integration of contact area over time to evaluate the reduction effect of surface design. They proposed a fine ring structure on a substrate and did systematic research on the geometry of the ring.

Inspired by Girard *et al.* [10], we propose a surface design with craterlike structures, which can effectively reduce the liquid-solid contact area and time by redirecting the lamella to spread into the air. This work can be seen as an extension of work of Girard *et al.* [10]. The surface we proposed here consists of concave structures that we refer to as craters in the following sections (see Fig. 3).

To investigate the drop dynamics, simulation methods such as volume of fluid [11], the lattice Boltzmann method [12], Multibody dissipative particle dynamics (MDPD) [13], and smoothed particle hydrodynamics [14] have all been applied in the literature. Compared to experiments, simulation methods have the general advantage of flexibility in observation and measurement. Among these methods, the Lagrangian formula owns unique advantages, as Zhao *et al.* [15] used it to successfully predict the depositing process of droplet impact. As a pure Lagrangian mesoscale method, MDPD can track the motion of fluid microelements, which means the transformation of the droplet surface can be well simulated at the mesoscopic scale. It has been used to address problems including free liquid/vapor interfaces [16–19]. The details of this method can be found in the Methods section.

This study aims to minimize the contact area and time by decorating the substrate with craterlike structures. We show a properly designed crater can redirect the droplet momentum and force it to spread into the air instead of along the substrate, thus effectively reducing the liquid-solid contact area and time simultaneously. Then we investigate the influence of crater radius and depth and the droplet landing location. Furthermore, we show a design of the crater array surface and examine the performance at some characteristic landing locations.

II. METHODS AND VALIDATION

A particle-based simulation method dissipative particle dynamics (DPD) is used in this study. Similar to a molecular dynamics system, a DPD model consists of many interactive particles governed by Newton's equation of motion

$$m_i \frac{\mathrm{d}^2 \mathbf{r}_i}{\mathrm{d}t^2} = m_i \frac{\mathrm{d}\mathbf{v}_i}{\mathrm{d}t} = \mathbf{F}_i = \sum_{j \neq i} \left(\mathbf{F}_{ij}^C + \mathbf{F}_{ij}^D + \mathbf{F}_{ij}^R \right), \tag{1}$$

where m_i is the mass of particle i, and t denotes time. The bold symbols $\mathbf{r}_i$ and $\mathbf{v}_i$ are position and velocity vectors of particle i, and $\mathbf{F}_i$ is the total force acting on particle i due to the presence of neighboring particles. The computing $\mathbf{F}_i$ is carried out over all neighboring particles within a cutoff range. Beyond the cutoff range, the interactions are negligible. The pairwise force consists of three parts: the conservative force $\mathbf{F}_{ij}^C$, the dissipative force $\mathbf{F}_{ij}^D$ and the random force $\mathbf{F}_{ij}^R$, which are in the forms, respectively:

$$\begin{aligned} \mathbf{F}_{ij}^C &= a_{ij} \omega_C(r_{ij}) \mathbf{e}_{ij}, \\ \mathbf{F}_{ij}^D &= -\gamma_{ij} \omega_D(r_{ij}) (\mathbf{v}_{ij} \mathbf{e}_{ij}) \mathbf{e}_{ij}, \\ \mathbf{F}_{ij}^R \cdot \mathrm{d}t &= \sigma_{ij} \omega_R(r_{ij}) \mathrm{d}\tilde{W}_{ij} \mathbf{e}_{ij}, \end{aligned} \tag{2}$$

where $r_{ij} = |\mathbf{r}_{ij}| = |\mathbf{r}_i - \mathbf{r}_j|$ is the distance between two neighboring particles i and j, $\mathbf{e}_{ij} = \mathbf{r}_{ij}/r_{ij}$ is the unit vector, and $\mathbf{v}_{ij} = \mathbf{v}_i - \mathbf{v}_j$ is difference of their velocities; $\mathrm{d}\tilde{W}_{ij}$ is an independent increment of the Wiener process [20]. The coefficients a_{ij}, γ_{ij}, and σ_{ij} determine the strength of each force, respectively. To satisfy the fluctuation-dissipation theorem [20] and to maintain the DPD system at a constant temperature [21], the dissipative force and the random force are related by $\sigma_{ij}^2 = 2\gamma_{ij} k_B T$

and $\omega_D(r_{ij}) = \omega_R^2(r_{ij})$. Warren [22] modified the conservative force term to include both a repulsive force and an attractive force, and established the MDPD. The repulsive force of MDPD depends on a weighted average of the local density, whereas the attractive force is density independent,

$$\mathbf{F}_{ij}^C = A_{ij} w_c(r_{ij}) + B_{ij}(\rho_i + \rho_j) w_d(r_{ij}). \tag{3}$$

Because a DPD model with a single interaction range cannot maintain a stable interface [23], the repulsive contribution in Eq. (3) is set to act within a shorter range $r_d < r_c$ than the soft pair attractive potential. The many-body repulsion is chosen in the form of a self-energy per particle, which is quadratic in the local density, $B_{ij}(\rho_i + \rho_j) w_d(r_{ij})$, where $B > 0$. The density of each particle is defined as $\bar{\rho}_i = \sum_{j \neq i} w_\rho(r_{ij})$ and its weight function w_ρ is defined as $w_\rho = \frac{15}{2\pi r_d^3}(1 - \frac{r}{r_d})^2$, where w_ρ vanishes for $r > r_d$.

The parameters used in this study are as follows: $A_{ll} = -80$, $B_{ll} = 20$, $A_{ls} = -5$, $B_{ls} = 20$, $r_c = 1.0$, $r_d = 0.75$, $\gamma_{ll} = 0.5$, $\gamma_{ls} = 0.5$. A and B are parameters in Eq. (3), and they control the attractive and repulsive force between MDPD particles, respectively. r_c and r_d are cutoff range of attractive and repulsive force in Eq.(3). γ controls the MDPD fluid viscosity. Subscript ll or ls indicates the parameter is applied to liquid-liquid interaction or liquid-solid interaction. These values are widely used MDPD parameters for liquid/vapor systems, and more details on choosing the parameters can be found in Arienti *et al.* [24].

The measured liquid properties are as follows in DPD units: density is 10.91, dynamic viscosity is 27.25, surface tension is 49.82, contact angle is around 150°. The droplet contains 272625 DPD particles with radius 18.1. The default impact velocity is 4.0, which leads to We = 126.3. Other dimensionless numbers are Re = 57.97, Ca = 2.18, Oh = 0.19. To ensure the no-slip boundary condition and no penetration of liquid particles into the solid structure, we adopt the boundary condition method for arbitrarily complex geometries proposed by Li *et al.* [25].

To quantitatively evaluate the influence of the contact time and contact area, we follow Girard *et al.* [10] to use the interaction parameter, I, which is the integral of the liquid-solid contact area over time [10]:

$$I = \int_0^T A(t) dt, \tag{4}$$

where $A(t)$ is the contact area at time t, and T is the overall contact time. We set the I with a plane surface as the reference I_0. Then we could easily learn the reduction effect of a new solid surface by comparing I with I_0. The $A(t)$ is measured by counting the liquid particles within the unit length range of solid particles and dividing it by the liquid density. This is an advantage of DPD compared to experiments, which can only infer the contact area indirectly with many difficulties such as the limitation of view and the distortion from liquid.

The DPD simulation results can be viewed in different ways (Fig. 1). The subplot (c) is a rendered picture of triangle surface mesh (b) which is constructed from the original DPD particles (a). All three renderings are used throughout the paper.

To validate the computational model, we compare the simulation results with experimental data from Girard *et al.* [10] (Supplemental Material movie S2 [28]) with the same droplet size, ring size, and We number. The explicit DPD scaling relationships for this case can be derived as follows: $l^{\mathrm{DPD}} = 5.56 \times 10^{-5} m$, $m^{\mathrm{DPD}} = 1.572 \times 10^{-11} kg$ and $t^{\mathrm{DPD}} = 1.04 \times 10^{-4} s$. Any values in dimensionless DPD units can be converted to physical dimensional properties using these relationships, and vice versa. Snapshots of the droplet in different stages are plotted with time stamps in Fig. 2.

The results show DPD simulation captures the different stages of this process quite well. The droplet forms a water bowl after rejected by the ring, then retracts to a similar shape and liftoff. Different from the experimental captured image, DPD results suffer from no motion blur and have access to all perspective camera angles.

We need to note that even the general liquid shape is consistent from one DPD simulation to another, the specific shape details are usually not the same. Because of the particle nature of DPD

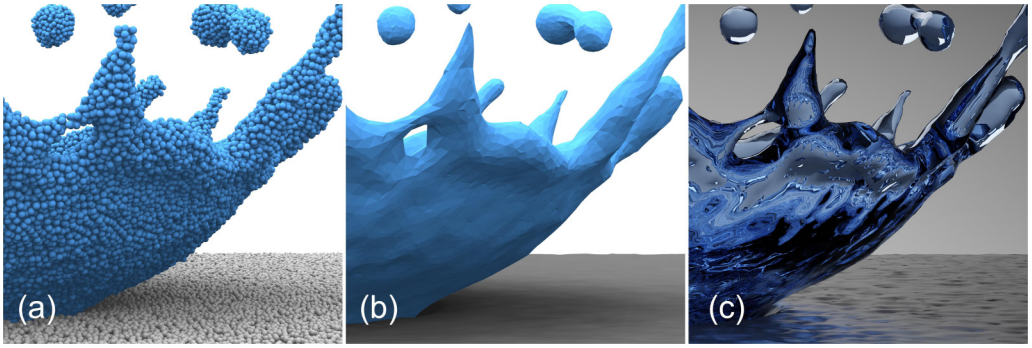

FIG. 1. Three different renders of the simulation result. (a) Particle view; (b) Mesh view; (c) Ray-tracing render view. The DPD simulations directly provide liquid particles position information (a); then, we reconstruct the surface mesh by identifying different clusters and the particles near the surface (b); last, we render the mesh by adding light, material, etc. (c).

and the inherent random force, the details of highly deformed droplet shape are very sensitive to the initial particle configuration and the random number we used in the DPD model. For example, the number and position of the tips in the Fig. 2(g) are not guaranteed for different DPD simulation, and the asymmetric contracting shape in the Fig. 2(h) are usually different if we change the random seed. Actually, we have run 8 DPD simulations for this comparison case and choose the most similar case to the experimental image provided. The only difference between the 8 DPD simulations is the random number generator seed as simulation inputs. In other words, the shape shown in Fig. 2(h) is selected on purpose, while other DPD simulations show generally similar outputs.

In Figs. 2(g) and 2(h), many small blue particles or clusters are flying in the air, which are sprays generated from the violent impact. Through cluster analysis, we conclude that despite their large numbers, the mass of the sprays is less than 1% of the whole droplet. So, we neglect the small mass change in this study.

The measured I/I_0 of DPD simulation is 29%, compared to the experimental result of around 25%. Overall, the DPD results agree with the data from Girard *et al.* [10], while some discrepancy remains which could result from many reasons. For example, the implementation of measuring the

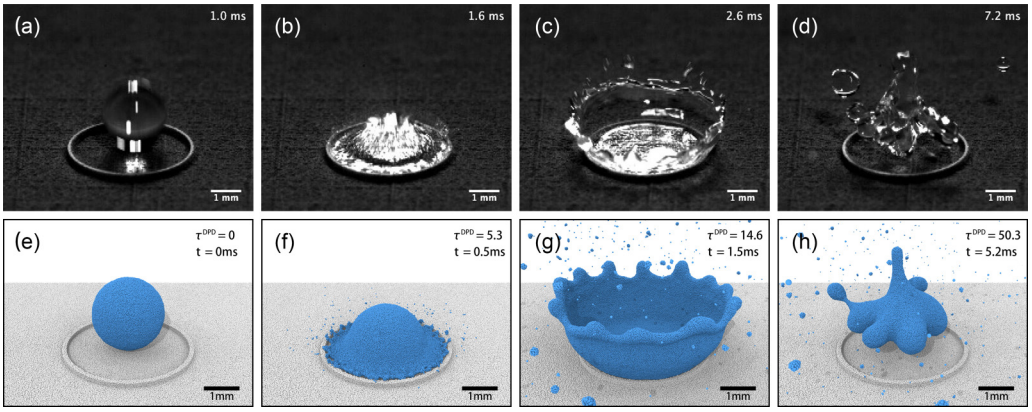

FIG. 2. The comparison of experimental images and DPD simulation results. (a)–(d) Experimental snapshots of a droplet impacting a superhydrophobic surface decorated with a ring structure. The droplet stretches into the air and forming a three-dimensional water bowl. Finally, the droplet retracts and liftoff. (e)–(h) DPD simulation snapshots. The DPD results generally capture the shape evolution in different stages.

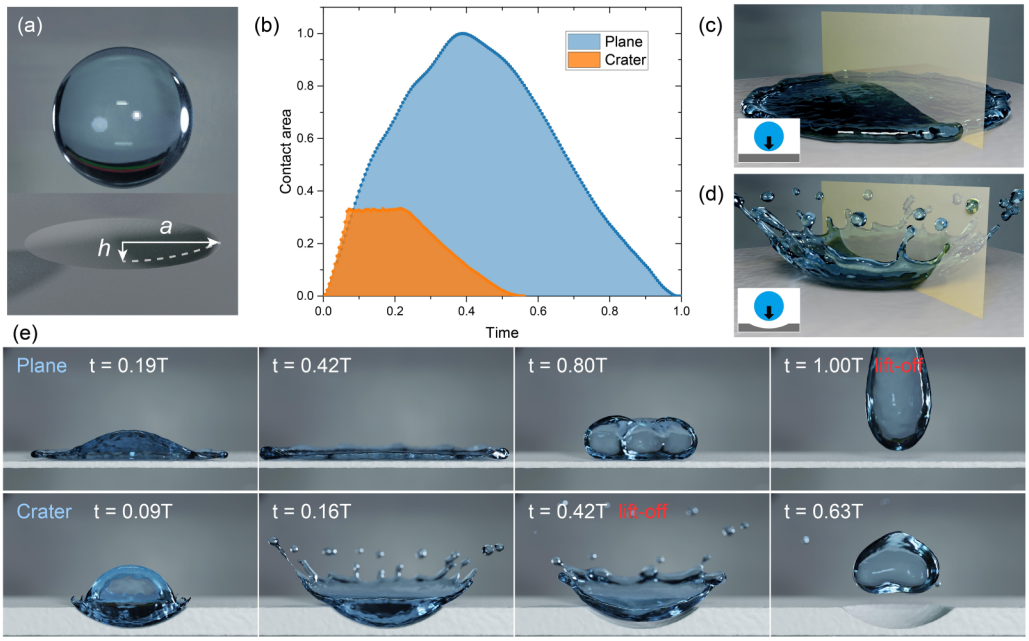

FIG. 3. (a) Illustration of the craterlike surface. (b) Comparison of contact area and contact time on a plane surface and craterlike surface. The contact area and time are both normalized. (c),(d) Droplet spreads to lamella along the plane surface but spread into the air on the craterlike surface. (e) Cross-section images of a droplet impacting on plane and craterlike substrate. Half of the crater and half of the droplet are hidden to observe the liftoff clearly. On the craterlike surface, the wetting area is much smaller, and the liftoff is earlier.

contact area, the different incompressibility between DPD liquid and real water (DPD liquid is less incompressible), the surface wettability difference.

III. RESULTS AND DISCUSSION

Throughout the paper, the craterlike substrate is obtained by trimming a plane surface with a spherical cap. The craterlike shape can be controlled by two parameters: radius a and depth h, as shown in Fig. 3(a).

Figure 3(b) shows the evolution of the contact area as a function of time. The blue and orange colors indicate plane surface and craterlike surface, respectively. The contact area and time are both normalized by the maximum value on the plane surface. The area below the curve corresponds to the impact parameter I in Eq. (4). We note for craterlike surface, the maximum contact area is significantly reduced, and the contact time is shortened as well. Figs. 3(c) and 3(d) are snapshots that impact plane and craterlike surface, respectively. Figure 3(e) are snapshots time series. The results are presented in a cross-section view to monitoring the contact between liquid and solid. On the plane surface, the droplet spreads over the surface until it reaches a maximum radius; then, due to surface tension, the liquid recedes. The dynamics are controlled by subtle balances between inertia, viscosity, and capillary forces [26]. Because the impact is performed on a superhydrophobic surface, the drop rebounds after retraction [27]. On the other hand, droplets impacting on craterlike surface can gain extra upward momentum. That can redirect the droplet to spread mainly in the air and detach from the substrate earlier.

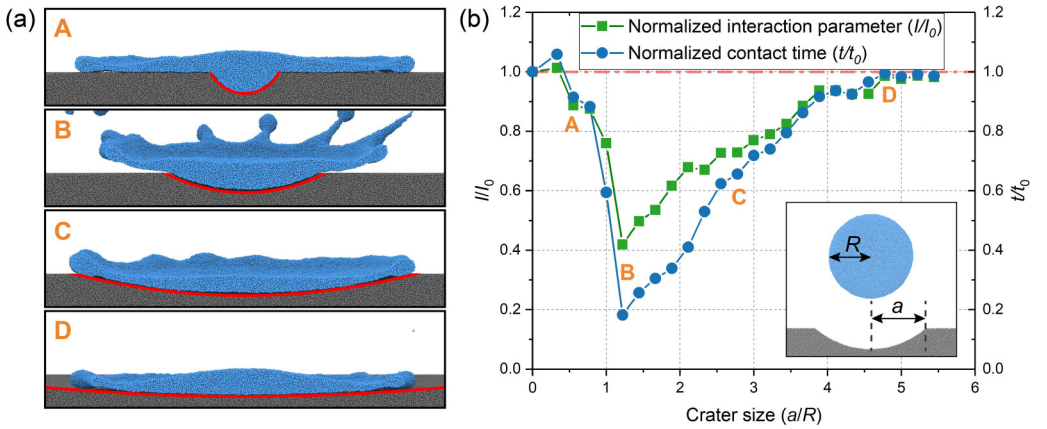

FIG. 4. The effect of crater radius (a in inset plot) on interaction parameter (I) and contact time (T). The a ranges from 0 (plane) to $5.5R$ (larger than the droplet). (a) Four representative liquid shapes. If the crater is too small (case A), the liquid overrun and spread along the substrate; once the size is in an optimized range (case B), the droplet would be redirected to spread in the air; if the crater radius is bigger than the size of maximum spreading lamella (case C and D), the droplet hardly spread in the air. (b) The measured I and T versus crater radius. All values are normalized by I_0, T_0, and R, respectively. There exists a minimum I/I_0 at $a = 1.22R$, and the T/T_0 share the similar trend. The results indicate to achieve the best performance of reducing the contact, the crater radius should be slightly bigger than the droplet radius (around $1.2R$).

A. Crater radius's effect

To start with, we investigate the effect of the crater radius [in Fig. 3(a)] on the contact area and time. The inset plot in Fig. 4(b) illustrates the setup. For easy comparison, all lengths are normalized by the droplet radius R. We change a from 0 (no crater) to $5.44R$ (bigger than the maximum spreading lamella on plain surface) while keeping the depth of crater $h = 0.33R$. The corresponding virtual sphere used to trim the substrate ranges from 0 to $803.33R$, respectively. Figure 4(a) shows four cross section views, and the red curves depict the shape of the crater bottom. The impact velocity keeps the same in all cases, which results in dimensionless number $\mathrm{We} = 126.2$.

Figure 4(b) summarized the measured interaction parameter I and contact time T versus the crater radius a. When a is smaller than R (case A), the droplet overruns and spreads horizontally on the plane, which is undesirable. Once a is bigger than R, the crater change the direction of spreading lamella noticeably, and the I/I_0 reached the minimum at $a = 1.22R$ (case B). In this optimized case, the overrun is eliminated, and the bouncing time is shortened, both contributing to the reduction effect. Continuing to increase a would jeopardize the effect of spreading into the air (case C and D) since the maximum spreading lamella hardly reaches the crater edge, and the redirected momentum is weakened.

Here, we take the advantage of the numerical investigation to take a closer look at the rather sharp transition between the overrun and the ejection phenomenon when the crater is a little bigger than the droplet. Considering the water bowl is basically rotationally symmetrical, we divide the domain into cylindrical bins and average the radial velocity and z velocity of particles in each bin. Figure 5 shows an overrun case and an ejection case. Each case has three snapshots presenting different stages. The space covered with black represents the solid substrate. The velocity vectors are colored and scaled by their magnitude. To outline the liquid shape, we average the particle number density in each bin and color in the space occupied by liquid with grey color. The only difference between the overrun and ejection cases is the radius of the crater. The crater radius is $1.0R$ and $1.4R$ for overrun and ejection, respectively. The depth of the crater is $0.3R$ for both cases.

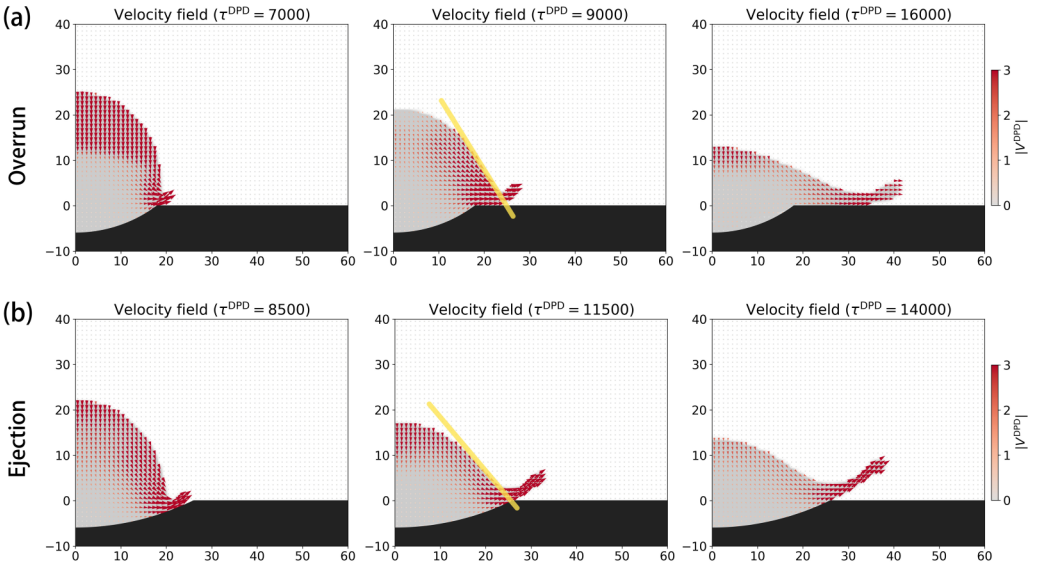

FIG. 5. Different crater radius leads to overrun or ejection phenomenon. (a) Overrun when $a/R = 1.0$; (b) Ejection when $a/R = 1.4$. The yellow line indicates the slope of the main body of liquid, showing where the surface's downward momentum hits.

In the overrun case, we notice the crater does provide upward momentum when the liquid encounters the barrier, but then the main body of droplet going outwards and downwards suppresses the rising lamella. Finally, the downwards momentum dominates the lamella and force it to touch the substrate. In the ejection case, the crater first lifts the precursor lamella; then the downward momentum of the main body mainly hits inside the crater, resulting in more ejection towards the air after the crater lift; finally, the lamella is freely stretched in the air. One key difference between overrun and ejection is where the huge downwards momentum of the main body surface hits. Through the velocity field plotted, we know the inner part of droplet has a near-zero velocity after contacting the bottom, while the surface part is actively flowing outwards and downwards at relatively high speed. We added yellow lines as guides to the eye for the surface momentum. In the overrun case, the momentum directly hits the in-the-air lamella, skips the crater and thus skips the opportunity to gain upward momentum. In the ejection case, the downwards momentum hits inside the crater, thus the crater is still effective to provide upward momentum. Overall, in the overrun scenario, the crater only affects the beginning part of the spreading, while in the ejection scenario, the crater provides the upward momentum for more liquid over a longer time.

B. Crater depth's effect

Next, we investigate how the crater depth h influences the contact. We test h from $0.05R$ to $1.0R$, while keeping $a = 1.22R$ (the best parameter from previous experiments). Figure 6(a) shows four representative liquid shapes. Case A is the benchmark of horizontal spreading on a plane substrate. Once the depth of the crater reaches $0.1R$ (Case B), the measured I/I_0 is dramatically reduced to about 60%; $h = 0.22R$ (Case C) would cut the I/I_0 by 70%. However, continuing to deepen the crater (Case D) seems to have no pronounced effect. Figure 6(b) plots the I/I_0 and T/T_0 as a function of the normalized crater depth (h/R). We can infer that the depth of crater has a direct influence on the I/I_0 and T/T_0. It controls the upward momentum of spreading, and can constrain the wetting area to the crater. However, once the overrun is eliminated ($h/R \sim 0.4$), the contact area remains nearly constant, and the reduction effect can hardly be improved further.

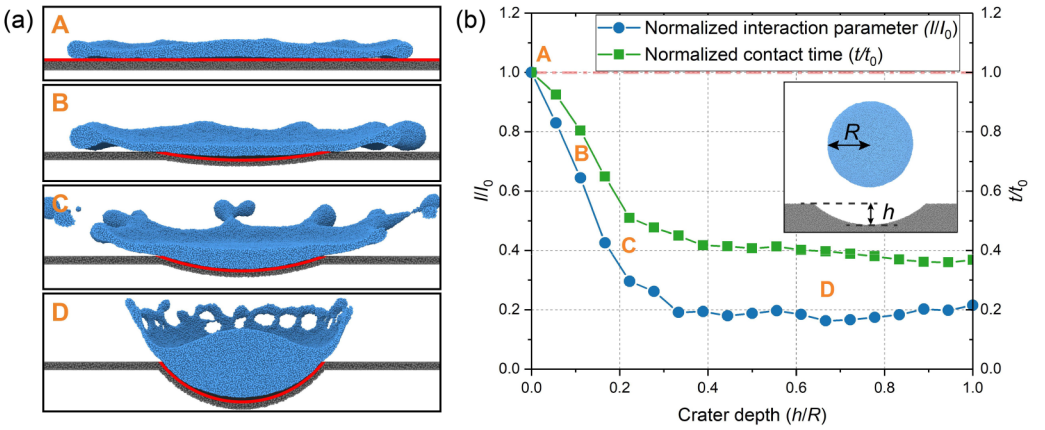

FIG. 6. The effect of crater depth (h in inset plot) on I and contact time T. The h ranges from 0 (plane) to $1.0R$. (a) Four representative liquid shapes. Hitting a plane surface (case A), the liquid will spread along the substrate; Even on a very shallow crater (case B), the droplet can gain noticeable upward momentum to detach when spreading; however, some overruns appear. Deepen the crater a little (case C), then none of the surface outside the crater is wetted. Once the spreading is entirely in the air, a deeper crater (case D) hardly improves the performance. (b) The measured I and T versus crater depth. All values are normalized by I_0, T_0, and R, respectively. The results indicate crater depth should be above a threshold to achieve the best performance of reducing the contact.

Figure 7 shows droplets spreading on craters with different depths. For the $h/R = 0.16$ case (overrun). The lamella only gains limited upwards momentum from the crater because the angle of the crater edge is very small. Then the weak upwards lamella is suppressed by the big downward

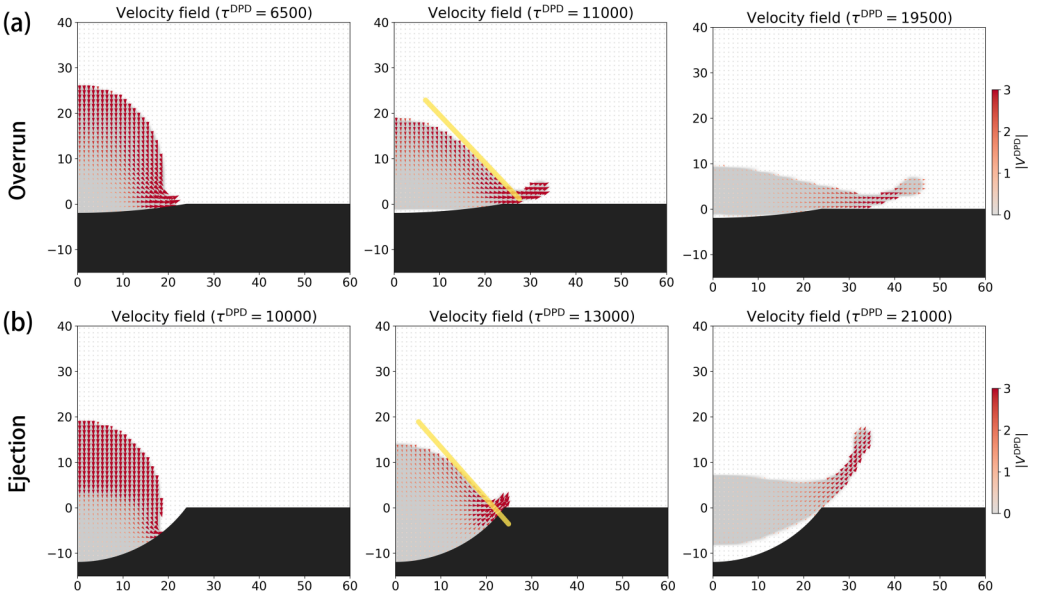

FIG. 7. Different crater depths lead to overrun and ejection phenomena. (a) Overrun as $h/R = 0.16$; (b) Ejection as $h/R = 0.6$. The yellow line indicates the slope of the main body of liquid, showing where the surface's downward momentum hits.

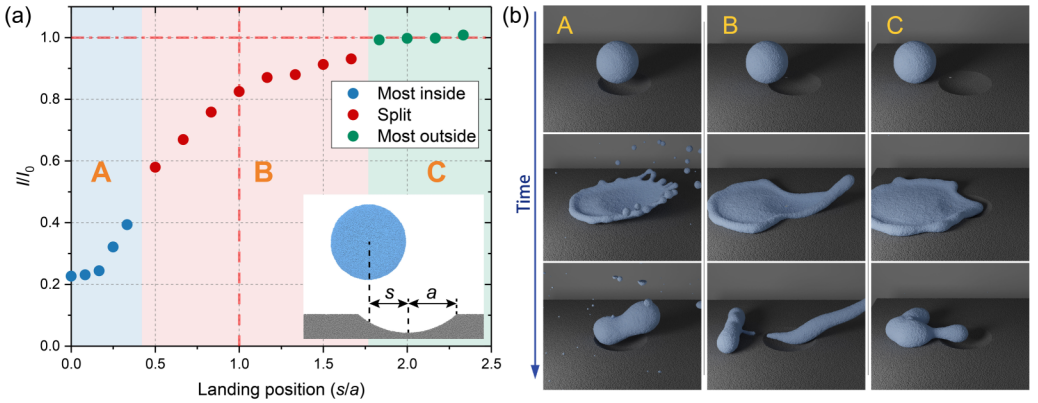

FIG. 8. The effect of landing location (off-center distance s) on I and T. The landing location ranges from crater center ($s = 0$) to far from crater ($s = 2.33a$). (a) The measured I and T versus s. The values are normalized by I_0, T_0, and a, respectively. The I/I_0 increase from around 0.2 (at the center) to 1.0 (far from the crater) monotonous as the effect of redirecting the droplet is diminished. That indicates to achieve the best performance, landing far off-center should be eliminated. (b) Three representative snapshots time series showing different liquid shape evolution.

momentum of the main body, resulting in an overrun lamella. For the $h/R = 0.6$ case (ejection), compared to $h/R = 0.16$, one difference is that the big angle of the crater edge induces strong upwards momentum for lamella, another difference is that when the lamella spread out, the slope of the main body surface does not hit the flying lamella. Both factors contribute to the forming of a spreading water bowl.

C. Off-center landing

In the above numerical experiments, the droplets are controlled to land at the center of the crater. Next, we investigate the effect of off-center landing. Parameters such as crater size ($a = 1.22R$), depth ($h = 0.22R$), and impact velocity (We = 126) stay the same throughout this section. Because of the symmetry of the crater, the landing location is represented by the off-center distance s [see Fig. 8(a)]. We measure the I/I_0 when s ranges from 0 to $2.33a$ and summarized the results in Fig. 8(a). We notice that once the landing location deviates from the crater center, the reduction effect begins to be undermined. We divide all the cases into three scenarios based on the gap in I/I_0 curve and the corresponding different types of shape evolution. Three representative shape evolution are shown in Fig. 8(b). In the first scenario [case A in both Figs. 8(a) and 8(b)], the landing point is near the center. The spreading shape is a mix of lamella and water bowl, and then the liquid contracts to a peanut shape and lifts off. In the second scenario (case B), the landing point is near the crater edge, nearly half of the droplet hits the crater and half hits the plane. The inertia of the two parts competes and finally tears the droplet apart. Due to surface tension, two separate small droplets are formed later. In the third scenario (case C), the majority of droplet hit outside of the crater. Since the crater does not provide enough influence to change the droplet momentum, the spreading is mainly horizontally. The droplet finally retracts to one piece and lifts off the ground. In Fig. 8, I/I_0 monotonically increase as s increases, which indicates in order to achieve a better contact reduction performance, a smaller gap between the landing point and crater center is desired.

D. Crater array

To consider a more real-world situation, we design a substrate constructed by overlapping craters. All craters lie in a square lattice, and their centers and radius are marked with grey dots and grey

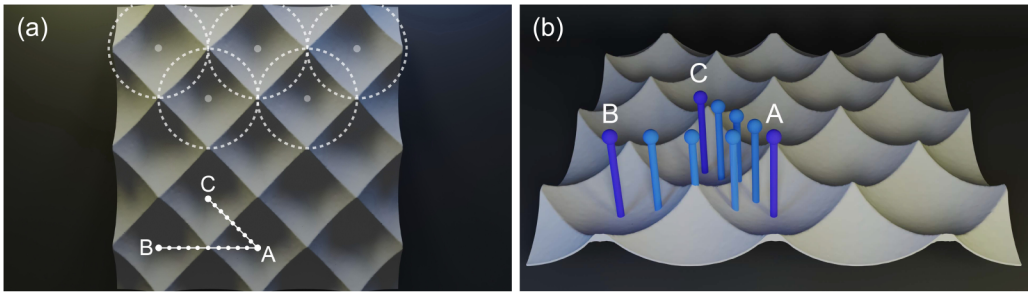

FIG. 9. A new design of substrate. The surface is trimmed by many spheres and forming a crater array. The craters are compactly packed to ensure no plain between craters. We test the I/I_0 and T/T_0 on different landing locations. The selected locations are on the path from one crater center A to its neighbor center B or C.

dashed circles, respectively (see Fig. 9). We choose this compact arrangement to eliminate the remaining plane between craters, which has been proven undesirable in the previous section.

Considering the crater fringe are trimmed by each other, we set the crater shape $a = 1.88R$, $h = 1.05R$ to achieve an effective optimal shape. Because the pattern is periodic, we only test I/I_0 on some representative landing locations. The selected locations lie on two paths: from crater center A to its neighbor center B, and from A to another neighbor center C, see Fig. 9(b). The AB path includes the peak point on substrate trimmed by four neighbor craters, and the AC path includes ridge points trimmed by two neighbor craters.

Figure 10(a) are the measured I/I_0 and T/T_0 versus landing locations on path AB (across the peak). s is the distance between landing location and crater center A, and AB is the distance between two centers. Because the substrate is symmetric to the peak point, we only show half of the results ($s/\mathrm{AB} \in [0, 0.5]$). The T and I are both normalized by the control case on a plane substrate. We notice that the trend of I is more complex than that on a single crater. Here, landing on the crater center still beats other locations regarding reduction in both I and T, while the worst I appears at $s = 0.43\mathrm{AB}$, and worst T appears at $s = 0.17\mathrm{AB}$.

Interestingly, I does not change in pace with T. This phenomenon originates from the versatile liquid spreading shape. Three representative cases are shown in Figs. 11(a)–11(c). When the droplet lands near the crater center (case a), the droplet produces two satellite droplets, and the two satellite drops detach the substrate very early due to the crater shape. When the landing location moves

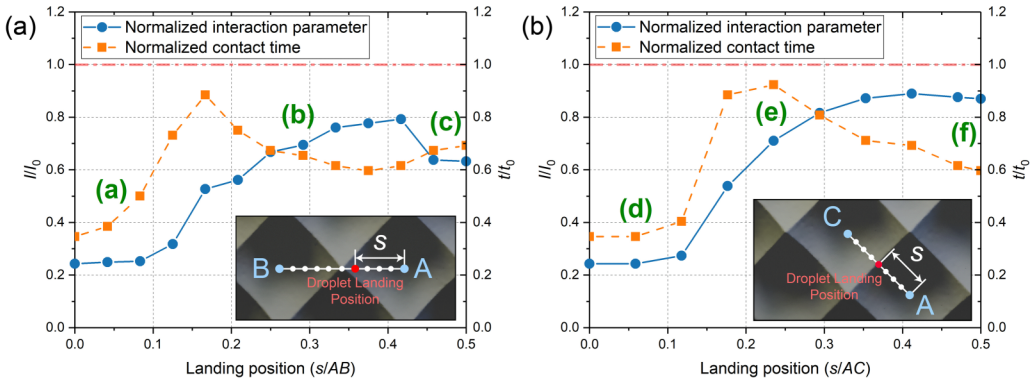

FIG. 10. The measured I/I_0 and T/T_0 versus landing location, (a) from A to B, (b) from A to C. The landing location is described by distance s normalized by distance AB or AC. Landing at the center still has the best performance; however, other landing locations all show reduced T and I.

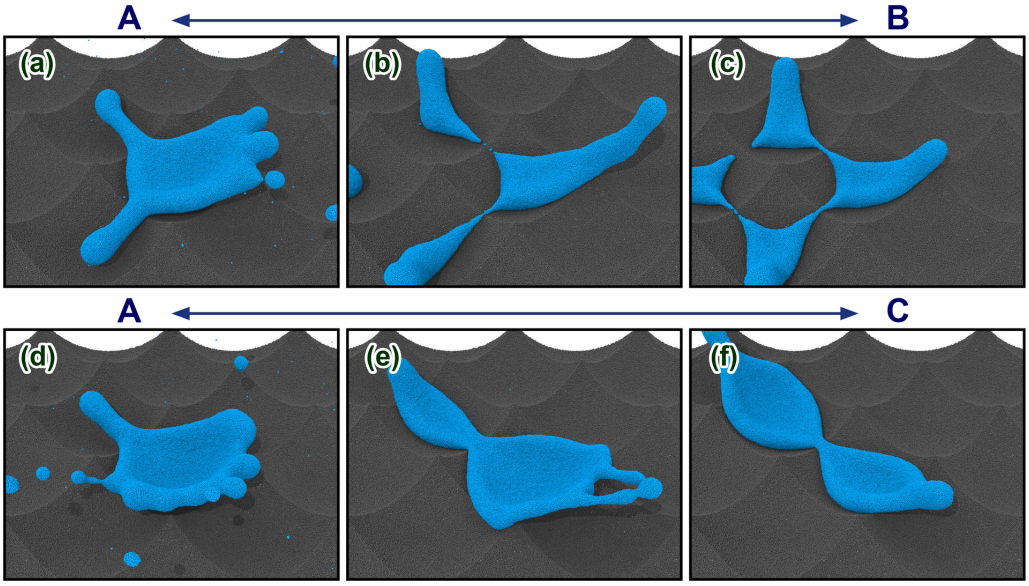

FIG. 11. Snapshots of six separate cases. The labels correspond to those in Fig. 10. The three cases in the first row are landing locations on path A-B, the three cases in the second row are on path AC. On path AB, the droplet may be broken by the peak trimmed by four craters; on path AC, the droplet may be divided into two parts by the ridge between two craters. The complexity of the shape evolution contributes to the asynchronous contact time and interaction parameter. However, all landing locations are effective in reducing contact area and time.

closer towards the peak point, the droplet starts to break into four parts and never retracts to one piece. The four parts are redirected to different directions (case c). The break happens very early, so the droplet does not go through the spread-retract-liftoff process, instead each part sliding along a different crater and move towards the air quickly.

Figure 10(b) are the results of I/I_0 and T/T_0 on path AC. The $s/AC = 0$ means landing on the crater center and $s/AC = 0.5$ means landing on the ridge. Similar to Fig. 10(a), deviating from the center in both directions increases the I/I_0. Here, the I/I_0 and t/t_0 show an opposite trend where $s \in [0.25\text{AC}, 0.43\text{AC}]$ in other words, the contact time decreases but the contact area increases more. Figures 11(d)–11(f) are snapshots of three different landing locations on path AC. Landing on the ridge split the droplet and result in a new slide-liftoff procedure instead of the conventional spread-retract-liftoff procedure. The sliding process helps droplets detach from the substrate earlier but increases the contact area from one crater to two craters. See the snapshots for comparison in Figs. 11(d)–11(f).

Overall, the I/I_0 on these selected landing locations fall in the range of 20% to 85%, relatively effective compared to a plane substrate.

IV. CONCLUSIONS

In this study, we showed that the contact area and time could be reduced simultaneously by decorating the superhydrophobic surface with crater-shape structures. The investigation done by MDPD showed that the crater structure could redirect the momentum of the droplet and lead it to spread towards the air instead of along the solid surface. We systematically investigated the effect of crater size and droplet landing location. The results showed the integration of contact area over time could be reduced by 75% if the crater structure is optimized and the droplet is landing at the crater center. In regards to off-center landing, the droplet tends to be split and follow a slide-liftoff

procedure instead of the conventional spread-retract-liftoff procedure. Finally, we mimic a more realistic scenario by duplicating the craters to an array and test some characteristic landing locations. All results indicate that the craterlike shape is effective in reducing the contact area and time. The present surface decoration may be useful in many applications where the heat transfer between droplets and solid surface needs to be minimized.

ACKNOWLEDGMENTS

The authors acknowledge the financial support from the National Natural Science Foundation of China (No. 12002242, No. 11902188, and No. 11872283), the Shanghai Science and Technology Talent Program (No. 19YF1417400), and the Fundamental Research Funds for the Central Universities (Grant No. 22120190207).

[1] Z. Zhao, D. Poulikakos, and J. Fukai, Heat transfer and fluid dynamics during the collision of a liquid droplet on a substrate-i. modeling, Int. J. Heat Mass Transf. **39**, 2771 (1996).

[2] J. C. Bird, R. Dhiman, H.-M. Kwon, and K. K. Varanasi, Reducing the contact time of a bouncing drop, Nature (London) **503**, 385 (2013).

[3] Y. Liu, M. Andrew, J. Li, J. M. Yeomans, and Z. Wang, Symmetry breaking in drop bouncing on curved surfaces, Nat. Commun. **6**, 10034 (2015).

[4] M. Abolghasemibizaki, R. L. McMasters, and R. Mohammadi, Towards the shortest possible contact time: Droplet impact on cylindrical superhydrophobic surfaces structured with macro-scale features, J. Colloid Interface Sci. **521**, 17 (2018).

[5] Y. Liu, L. Moevius, X. Xu, T. Qian, J. M. Yeomans, and Z. Wang, Pancake bouncing on superhydrophobic surfaces, Nat. Phys. **10**, 515 (2014).

[6] R. Zhang, P. Hao, and F. He, Rapid bouncing of high-speed drops on hydrophobic surfaces with microcavities, Langmuir **32**, 9967 (2016).

[7] V. Fink, X. Cai, A. Stroh, R. Bernard, J. Kriegseis, B. Frohnapfel, H. Marschall, and M. Wörner, Drop bouncing by micro-grooves, Int. J. Heat Fluid Flow **70**, 271 (2018).

[8] P. B. Weisensee, J. Tian, N. Miljkovic, and W. P. King, Water droplet impact on elastic superhydrophobic surfaces, Sci. Rep. **6**, 1 (2016).

[9] X.-M. Li, D. Reinhoudt, and M. Crego-Calama, What do we need for a superhydrophobic surface? A review on the recent progress in the preparation of superhydrophobic surfaces, Chem. Soc. Rev. **36**, 1350 (2007).

[10] H.-L. Girard, D. Soto, and K. K. Varanasi, Waterbowls: Reducing impacting droplet interactions by momentum redirection, ACS Nano **13**, 7729 (2019).

[11] M. Pasandideh-Fard, Y. Qiao, S. Chandra, and J. Mostaghimi, Capillary effects during droplet impact on a solid surface, Phys. Fluids **8**, 650 (1996).

[12] H. P. Jansen, K. Sotthewes, H. J. Zandvliet, and E. S. Kooij, Potential of lattice Boltzmann to model droplets on chemically stripe-patterned substrates, Appl. Surf. Sci. **361**, 122 (2016).

[13] Y. Wang, Y. Wang, and S. Wang, Droplet impact on cylindrical surfaces: Effects of surface wettability, initial impact velocity, and cylinder size, J. Colloid Interface Sci. **578**, 207 (2020).

[14] T. Jiang, J. Ouyang, B. Yang, and J. Ren, The sph method for simulating a viscoelastic drop impact and spreading on an inclined plate, Computat. Mech. **45**, 573 (2010).

[15] Z. Zhao, D. Poulikakos, and J. Fukai, Heat transfer and fluid dynamics during the collision of a liquid droplet on a substrate-ii. experiments, Int. J. Heat Mass Transf. **39**, 2791 (1996).

[16] C. Lin, S. Chen, L. Xiao, and Y. Liu, Tuning drop motion by chemical chessboard-patterned surfaces: a many-body dissipative particle dynamics study, Langmuir **34**, 2708 (2018).

[17] K. Zhang, Z. Li, M. Maxey, S. Chen, and G. E. Karniadakis, Self-cleaning of hydrophobic rough surfaces by coalescence-induced wetting transition, Langmuir **35**, 2431 (2019).

[18] Y. Wang and S. Chen, Droplets impact on textured surfaces: mesoscopic simulation of spreading dynamics, Appl. Surf. Sci. **327**, 159 (2015).
[19] C. Lin, L. Yang, F. Chen, S. Chen, and H. Yin, A dissipative particle dynamics and discrete element method coupled model for particle interactions in sedimentation toward the fabrication of a functionally graded material, Colloids Surf., A **604**, 125326 (2020).
[20] P. Espanol and P. Warren, Statistical mechanics of dissipative particle dynamics, EPL **30**, 191 (1995).
[21] R. D. Groot and P. B. Warren, Dissipative particle dynamics: Bridging the gap between atomistic and mesoscopic simulation, J. Chem. Phys. **107**, 4423 (1997).
[22] P. B. Warren, Vapor-liquid coexistence in many-body dissipative particle dynamics, Phys. Rev. E **68**, 066702 (2003).
[23] I. Pagonabarraga and D. Frenkel, Dissipative particle dynamics for interacting systems, J. Chem. Phys. **115**, 5015 (2001).
[24] M. Arienti, W. Pan, X. Li, and G. Karniadakis, Many-body dissipative particle dynamics simulation of liquid/vapor and liquid/solid interactions, J. Chem. Phys. **134**, 204114 (2011).
[25] Z. Li, X. Bian, Y.-H. Tang, and G. E. Karniadakis, A dissipative particle dynamics method for arbitrarily complex geometries, J. Comput. Phys. **355**, 534 (2018).
[26] D. Bartolo, C. Josserand, and D. Bonn, Retraction dynamics of aquous drops upon impact on nonwetting surfaces, J. Fluid Mech. **545**, 329 (2005).
[27] C. Josserand and S. T. Thoroddsen, Drop impact on a solid surface, Annu. Rev. Fluid Mech. **48**, 365 (2016).
[28] See Supplemental Material at https://pubs.acs.org/doi/abs/10.1021/acsnano.9b01301 for the experimental movie.